PHOTONICS Research

Radiation-pressure-induced photoluminescence enhancement of all-inorganic perovskite $CsPbBr_3$ quantum dots

Ying Zhang,[1,2] Haiou Zhu,[3] Taiwu Huang,[1] Zongpeng Song,[2] and Shuangchen Ruan[2,3,*]

[1]Center for Advanced Material Diagnostic Technology, College of Engineering Physics, Shenzhen Technology University, Shenzhen 518118, China
[2]Guangdong Provincial Key Laboratory of Mico/Nano Optomechatronics Engineering, College of Optoelectronic Engineering, Shenzhen University, Shenzhen 518060, China
[3]College of New Materials and New Energies, Shenzhen University of Technology, Shenzhen 518118, China
*Corresponding author: scruan@szu.edu.cn

Received 12 March 2019; revised 26 May 2019; accepted 26 May 2019; posted 28 May 2019 (Doc. ID 362245); published 12 July 2019

Perovskite quantum dots (QDs) are of great interest due to their outstanding optoelectronic properties and tremendous application potential. Improving photoluminescence (PL) spectra in all-inorganic perovskite QDs is of great importance for performance enhancement. In this work, the PL quantum yield of the $CsPbBr_3$ perovskite QDs is enhanced from 70% to 95% with increasing radiation pressure. Such enhancement is attributed to the increased binding energy of self-trapped excitons (STEs) upon radiation pressure, which is consistent with its blue-shifted PL and other characterization results. Furthermore, we study ultrafast absorption spectroscopy and find that the dynamics of relaxation from free excitons to STEs in radiation pressure $CsPbBr_3$ QDs is ascribed to stronger electron–phonon coupling in the contracted octahedral structure. It is further demonstrated that radiation pressure can boost the PL efficiency and explore effectively the relationship between the structure and optical properties.

https://doi.org/10.1364/PRJ.7.000837

1. INTRODUCTION

As is known, radiation pressure is the pressure exerted upon any surface due to the exchange of momentum between the object and the electromagnetic field. This includes the momentum of light or electromagnetic radiation of any wavelength that is absorbed, reflected, or otherwise emitted (e.g., black body radiation) by matter on any scale [1–3]. Radiation pressure is applied to the surface of the object, causing mechanical stress on the object. Radiation pressure was proposed by Maxwell in 1864 and confirmed by Lebedev in 1901. The forces generated by radiation pressure are important in some physical processes and can find their appealing applications in many areas related to the interaction between light and matter, which was confirmed by some research work in recent years [4–11]. It is a meaningful thing to continue to seek and explore new physical applications of radiation pressure.

Recently, inorganic perovskite materials have received extensive attention for their excellent optical properties, good stability, and low cost [12–21]. They have extensive applications in photovoltaic perovskite solar cells [22,23], light-emitting diodes [24–26], high-energy detectors [27–30], lasers [31–34], and other fields [35]. However, there are still some shortcomings that significantly influence their optical and optoelectronic properties and consequently, the device performance [36,37]. Improving photoluminescence (PL) spectra in all-inorganic perovskite quantum dots (QDs) is of great importance for high-performance perovskite devices. To enhance PL quantum yield (PLQY), a series of methods has been proposed recently, such as a solution-based hot-casting technique and an atomic substitution doping technique [38–43]. Among different mechanisms that improve the performance of inorganic perovskite, pressure-induced enhancement provides another attractive solution. Researchers Yasutaka *et al.* discovered that luminescence properties and stability of the perovskite could be improved by mechanical pressure, which induces regulation on the degree of octahedron distortion of the halogen perovskite [44–46]. Now that the radiation pressure is one kind of pressure, a similar positive phenomenon may also happen when interacting with perovskite. However, the effect of radiation pressure on the performance of inorganic perovskite QDs is less investigated. So the difference between the effects of radiation and mechanical pressure on the optical properties of matter is an interesting topic.

In this study, radiation pressure is exploited to enhance the performance of all-inorganic perovskite $CsPbBr_3$ QDs for the first time, as far as we know. All-inorganic perovskite $CsPbBr_3$ QDs were irradiated by the 400 nm femtosecond laser under different radiation pressures, and their optical performance to

radiation pressure was studied by *in situ* PL, time-resolved PL (TR-PL) decay, and femtosecond transient absorption spectroscopy (fs-TAS). It is found that the PLQYs of all-inorganic perovskite $CsPbBr_3$ QDs are apparently improved after radiation pressure by a 400 nm fs laser. The experiment confirms that radiation pressure is similar to mechanical pressure and can also improve the luminescence performance of the perovskite QDs. What is more, operating means of radiation pressure is more convenient than that of mechanical pressure. So, radiation pressure is proved to be useful in the improvement of optical performance of inorganic perovskite.

2. RESULTS AND DISCUSSION

The $CsPbBr_3$ QD mentioned here was synthesized following a recipe reported by Protesescu *et al.* with slight modification [47]. The $CsPbBr_3$ QD solution was dropped on a quartz substrate and spin-coated to obtain QD films and dried naturally in the ambient condition. The detailed fabrication process can be found in Sec. 3. The molecular structural model of $CsPbBr_3$ QDs is illustrated in the inset in Fig. 1(a) (left); it can be seen that the $CsPbBr_3$ QD has a cubic structure. Figure 1(a) shows the UV–vis absorption and PL spectra of the QDs we prepared. The PL peak was centered at 504 nm, with a bandwidth (full width at half maximum, FWHM) of 20 nm. As revealed by transmission electron microscopy (TEM), $CsPbBr_3$ QDs show cubic morphologies highly uniform with an average side length of 13 ± 1 nm and exhibit a well-defined morphology with good monodispersity [Fig. 1(b)]. The high-resolution TEM (HRTEM) images [top right insets in Fig. 1(b)] reveal that the original $CsPbBr_3$ QDs are highly crystalline and display lattice fringes with a spacing distance of 0.57 nm. In addition, the uniform distribution of the large area of $CsPbBr_3$ QD thin film was also confirmed by scanning electron microscopy (SEM)-energy dispersive spectrometer (EDS) elemental mapping (see Fig. 6 in Appendix A.2).

To study the effect of radiation pressure on the property of perovskite QDs, we conducted laser excitation experiments. The $CsPbBr_3$ QDs film was irradiated by a fs pulse laser of 400 nm with different power intensities; the repetition frequency was 1 kHz, pulse-width 35 fs, and laser focal spot diameter about 1 mm, and the intensity distribution of the laser beam was a non-uniform Gaussian distribution. According to calculation, in such a non-uniform Gaussian light field, the radiation pressure in the peak of pump is higher than mechanical pressure. The scale of force is proportional to the intensity gradient of the light, which is called the dipole gradient force or the induced radiation pressure, and its specific calculation process is shown in Appendix A.1 and Table 4 of Appendix A.1. As shown in Fig. 2(a), the emission peak was blue shifted by 7 nm from 504 nm to 497 nm at different radiation powers from 0.1 to 3 W, which correspond to peak radiation pressure from 0.06 GPa to 0.38 GPa. In the figure, we also find that the PL intensity gradually increases with the increasing radiation power; however, it does not necessarily mean that the increasing radiation pressure results in PL intensity enhancement. In order to testifyto the influence of radiation pressure on PL intensity, as shown in Fig. 1(d), under the same radiation power, the very moment of the beginning and the time of several minutes are compared, which shows an obvious luminescence enhancement in the radiation-pressure-processed sample. Those interesting phenomena are consistent with the trend under small pressure in the literature [44]. We study the effect of radiation pressure

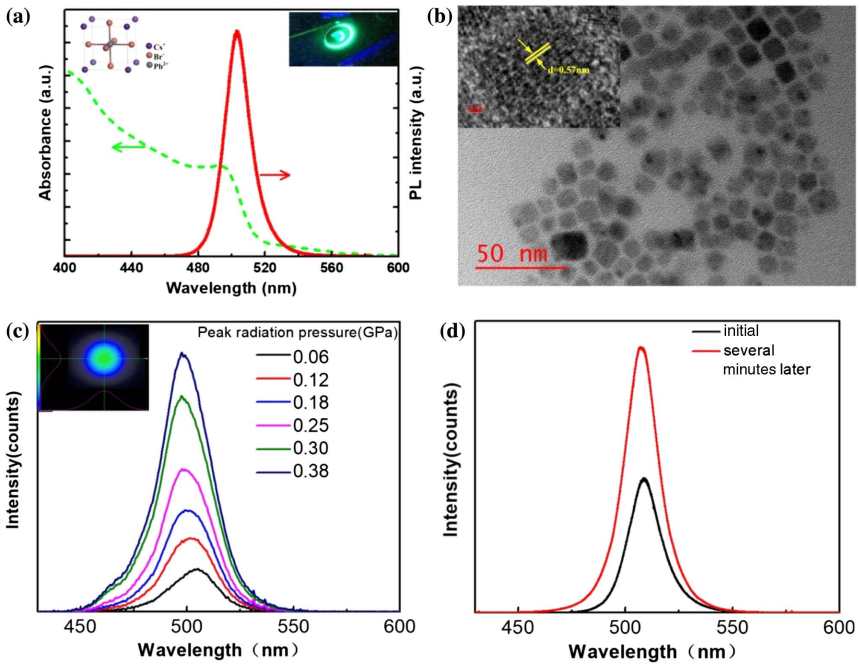

Fig. 1. (a) UV–vis absorption and PL emission spectra of $CsPbBr_3$ QDs. The inset shows the cubic perovskite structure of $CsPbBr_3$ (left) and schematic of perovskite $CsPbBr_3$ QDs after irradiation pressure (right). (b) TEM images of $CsPbBr_3$. The inset is the HRTEM image. (c) Changes in the PL spactra of $CsPbBr_3$ QDs under different radiation pressures of the laser. The inset shows the beam quality of non-uniform Gaussian distribution. (d) PL spectra of the original and radiation pressure-processed $CsPbBr_3$ QDs.

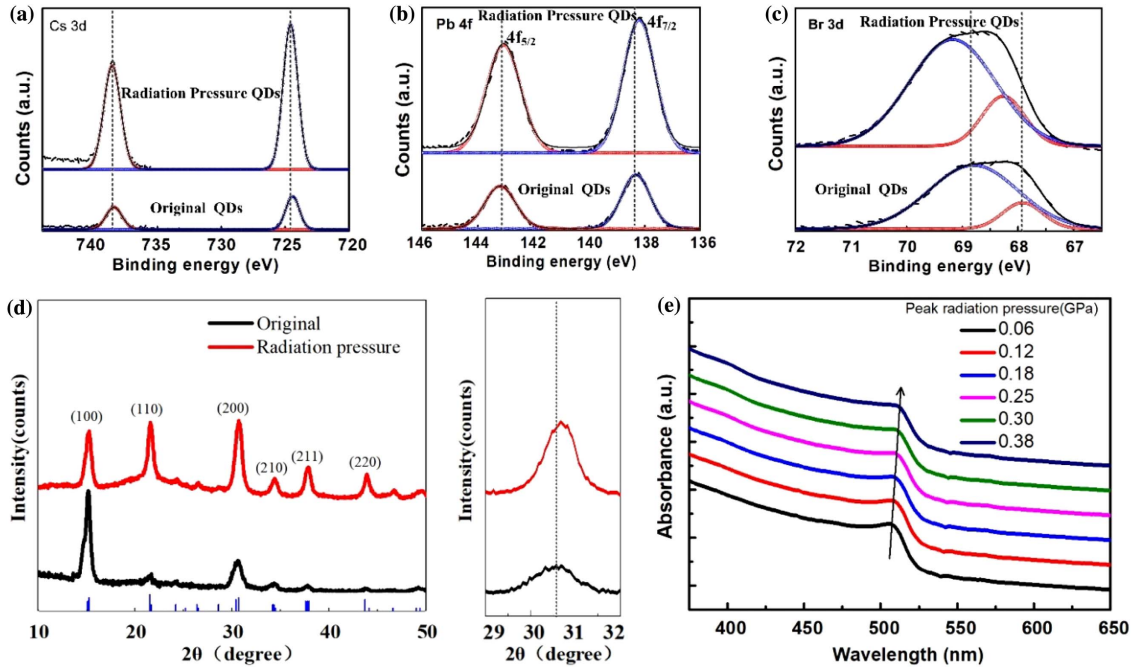

Fig. 2. XPS profiles corresponding to (a) Cs 3d, (b) Pb 4f, and (c) Br 3d of original and radiation pressure $CsPbBr_3$ QDs. (d) XRD patterns of perovskite $CsPbBr_3$ QDs with and without radiation pressure. The black line represents original QDs, and the red line represents radiation pressure QDs. The corresponding Miller indices are labeled at the top of the diffraction peaks. (e) Optical absorption of $CsPbBr_3$ QDs with increasing radiation pressure.

on the luminescence properties of perovskite QDs from two aspects: emission wavelength shift and luminescence intensity change.

A. Effect of Radiation Pressure on the Emission Wavelength Shift

In order to study the surface state situation, X-ray photoelectron spectroscopy (XPS) was conducted on $CsPbBr_3$ QDs under radiation pressure in comparison to that of original $CsPbBr_3$ QDs. Figure 2 shows XPS peaks of Cs, Pb, and Br on original and radiation pressure $CsPbBr_3$ QDs thin film. The high-resolution Cs 3d, Pb 4f, and Br 3d chemical states, which agree well with $CsPbBr_3$ QDs thin film, are shown in Figs. 2(a)–2(c), respectively. After radiation pressure, no change is found for Cs 3d peaks, indicating the low bonding interactions of Cs with Br ions in the crystal lattice [Fig. 2(a)]. Furthermore, the high-resolution XPS profiles [Fig. 2(b)] revealed that the binding energy of Pb^{2+} $4f_{5/2}$ and Pb^{2+} $4f_{7/2}$ in radiation pressure $CsPbBr_3$ QDs decreased in comparison to that of original $CsPbBr_3$ QDs, and the binding energy of Br 3d in radiation pressure $CsPbBr_3$ QDs increased in comparison to that of original $CsPbBr_3$ QDs, which are ascribed to the lattice contraction due to radiation pressure.

The X-ray diffraction (XRD) patterns of as synthesized $CsPbBr_3$ QDs [Fig. 2(d)] further show that both the original and radiation pressure $CsPbBr_3$ QDs possess cubic crystalline structure, indicating that the radiation pressure does not change the basic crystalline forms of QDs. However, as compared to the original QDs, a slight shift of the diffraction peak at (200) toward a higher angle was observed for the radiation pressure QDs [right panel of Fig. 2(d)], indicating the lattice contraction due to radiation pressure. Furthermore, the optical properties of the original and radiation pressure $CsPbBr_3$ QDs were revealed by steady-state UV–vis absorption. From the UV–vis absorption spectra [Fig. 2(e)], it can be clearly seen that the radiation pressure $CsPbBr_3$ QDs induced a slight blue-shift of the characteristic absorption edge of $CsPbBr_3$ QDs, because of the modulation in the electronic structure of QDs induced by radiation pressure. Moreover, the morphology and crystallinity of $CsPbBr_3$ QDs did not exhibit a distinct change before or after radiation pressure, which could be readily deduced from the TEM and HRTEM images, as shown in Fig. 7 in Appendix A.3. This phenomenon is quite similar to that in Ref. [45], and it leads to the blue-shift of the emission wavelength. However, the results of XPS and XRD show that the internal local structure of $CsPbBr_3$ QDs has been contracted in radiation pressure.

B. Effect of Radiation Pressure on the Intensity of PL

A self-trapped exciton (STE) represents a photo-induced electron–hole pair (exciton) mediated by the interaction between the exciton and the corresponding lattice, and the increased luminescence intensity may originate from an increase of the STE in perovskite materials under pressure [48–51]. In cases of strong coupling of electrons or holes to the crystal lattice, a carrier may be self-trapped as a small polaron in its own lattice distortion field. A bound electron–hole pair involving such a carrier is generally described as an STE, and it may dramatically influence luminescence, energy transport, and lattice defect formation in the crystal.

To obtain an intuitive understanding of the proposed mechanism, the corresponding dynamic processes in original (left) and

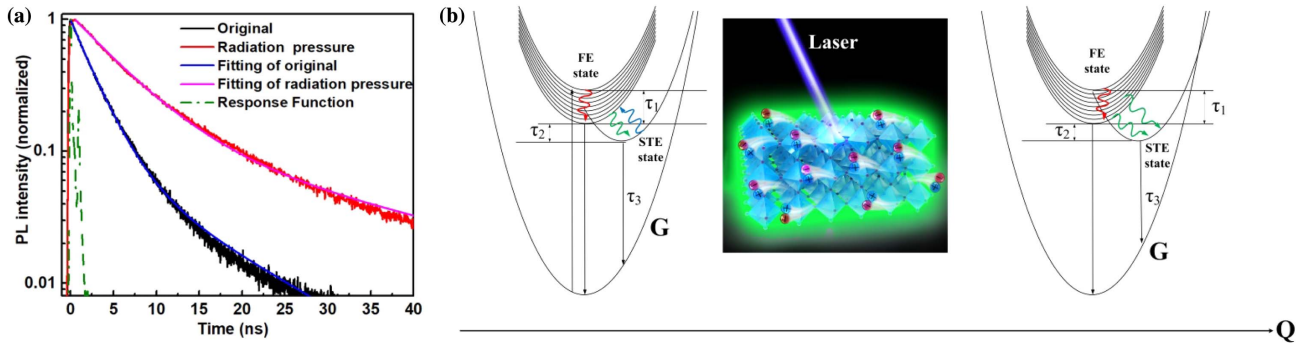

Fig. 3. (a) TR-PL decays for perovskite films with radiation pressure $CsPbBr_3$ QDs. (b) Schematic energy diagram of the EF and STE states in original (left) and radiation pressure (right) perovskite QDs.

radiation pressure (right) $CsPbBr_3$ QDs are schematically visualized in Fig. 3(a) (red arrows). In original $CsPbBr_3$ QDs, electrons transit from valence band to conduction band to form free excitons, and the excited carriers are readily localized to form bound excitons from the conduction band owing to strong quantum confinement from the unique structure of QDs. The formed bound excitons subsequently relax downward to the self-trapped state (green arrows). Due to the weak electron–phonon coupling under ambient conditions, the STE binding energy is relatively small, and a large number of excitons spontaneously change from self-trapping to the original bound excitons by thermal movement (blue arrows). After radiation pressure induces lattice contraction, the electron-phonon coupling is dramatically enhanced, and the STE binding energy is increased, so that more excited state carriers become stable STEs, and thereby self-trapping exciton recombination is largely enhanced. The radiation pressure effect regulates the interaction between the exciton and the corresponding lattice of the all-inorganic perovskite $CsPbBr_3$ free exciton, thereby improving the STE luminescence properties. It is found that radiation pressure can successfully induce a dipole moment of free excitons accumulating and the lattice vibration of $CsPbBr_3$ QDs. Accordingly, the fluorescence is gradually enhanced due to the formation of STEs from lattice vibration and non-uniform light field of radiation pressure:

$$A(t) = A_1 \exp(-t/\tau_1) + A_2 \exp(-t/\tau_2), \quad (1)$$

where A_1 and A_2 are the relative amplitudes, and τ_1 and τ_2 are the lifetimes for the fast and slow recombination, respectively [52]. The TR-PL decays are attributed predominantly to exciton radiative recombination. The bi-exponential decay result powerfully demonstrates that two different particles take part in the emission process, shown in Table 1. The PLQYs of original and radiation pressure $CsPbBr_3$ QDs are 70% and 95%, respectively, and from the different magnitudes of the radiation pressure on the effect of the PLQY of $CsPbBr_3$ QDs shown in Table 5 in Appendix A.1, the PLQYs under the radiation pressure $CsPbBr_3$ films are increased with larger radiation pressure. This is because the increasing radiation pressure for $CsPbBr_3$ QDs leads to more STEs and improves luminescence properties. The steady-state ensemble PL lifetime measurements of the radiation pressure $CsPbBr_3$ QDs showed long-lived charge carriers with a slow PL decay curve. The measured long lifetime of

Table 1. Lifetime Fitting Results of $CsPbBr_3$ QDs Sample

	Original QDs		After Radiation Pressure	
	Value (ns)	Relative (%)	Value (ns)	Relative (%)
τ_1	2.624 ± 0.096	91	3.771 ± 0.095	88
τ_2	11.45 ± 0.145	9	20.1 ± 0.941	12
τ_{avg}	3.42		5.75	

≈20 ns was almost double the lifetime of the original QDs [Fig. 3(a) and Table 1] and also dramatically longer than that of the original QDs. The results indicate that the short lifetime of several nanoseconds can be explained by the originally generated excitons recombination upon light absorption, while the long-lived component can be attributed to the excitons recombination being connected with STE due to the stable excitons at ambient conditions [53]. In addition to radiation-pressure-induced surface reconstruction, the PL enhancement and longer lifetime also explained the single-crystallinity phase with minimal defects of the pressure-synthesized QDs that had a low probability of recombination with the photo-generated exciton [54]. Since the large lifetime of radiative recombination corresponds to high PLQYs, the result shows that the proportion of excitons participating in the radiation recombination is significantly more than that of the original QDs, implying the radiation-pressure-driven increase in STEs agrees well with the changes of PL intensity.

The mechanism behind such an improvement is explained and discussed as follows. Considering the higher quantum yield of exciton luminescence in radiation pressure $CsPbBr_3$ QDs, the octahedral structure vibrations of radiation pressure are more likely to cause structural reorganization of the photo-induced excited state. This leads to the enhanced intensity of electron–phonon coupling under radiation pressure, which increases the STEs' binding energy, and the STEs cannot transmit to bound excitons by thermal activation. Since the STEs are usually formed by exciton and lattice vibration interaction, the enhanced electron–phonon coupling here can effectively bind the photoexcited electron–hole pairs and easily form STEs. This will promote the concentration of STEs and boost the possibility of radiative recombination of STEs. Such a dynamic process illustrated here is similar to that in Refs. [50,55]. Thus, lattice slight contraction results in a significant increase of

electron–phonon coupling strength under radiation pressure, and a persistent increase in PL intensity can be observed with radiation pressure.

In addition, to elucidate the origins of radiation-pressure-induced emission, fs time-resolved TAS was measured from the comparative analysis of the exciton relaxation dynamics in $CsPbBr_3$ QDs with and without radiation pressure. Figure 4 compares the transient absorption ΔA data obtained from original and radiation pressure $CsPbBr_3$ QDs under identical experimental conditions including sample concentration and pump intensity 8 $\mu J/cm^2$. In the fs-TA measurements, we adopted a pump–probe configuration featuring a UV pump (400 nm), which is suited to induce an interband transition for both samples.

In order to understand the carrier behavior of electron holes in semiconductors more clearly, the characteristic dynamics and transient spectroscopy from the graph are extracted. The left graph in Fig. 4(a) gives the temporal evolution spectral behavioral characteristics of the original sample at several representative probe delays ranging from 0.1 ps to 1 ns. We can clearly see that its spectral behavior has two bands. For the high-energy band, a light-induced bleaching negative signal quickly reaches a negative maximum in 3 ps, and then slowly returns to positive through the zero point, reaching the maximum value of the light-induced excited state absorption, and then evolving after a long decay time. According to Mondal and Samanta's spectral assignments in a comprehensive fs-TA study on the exciton dynamics of $CsPbBr_3$ QDs, we can safely attribute the two negative probe bleach (PB) profiles, labeled PB1 and PB2, to the ground-state bleach and the hot-exciton-induced bleach, respectively [56].

For the low-energy band, the fast delay time of 1 ps reaches the maximum positive signal of excited state absorbed, and then decays at a long relaxation time and a complicated process. Figure 4(b) shows TA spectra and kinetics of laser radiation pressure $CsPbBr_3$ perovskite QDs at different delay times, and

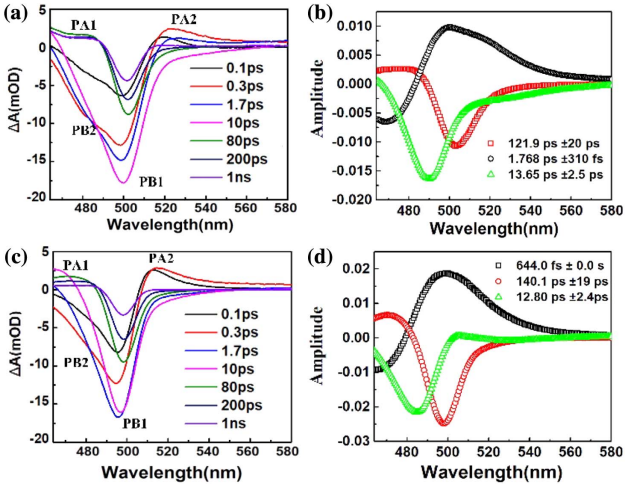

Fig. 4. (a) fs-TA spectra (excitation 400 nm) taken at several representative probe delays and (b) decay-associated spectra (DAS) for the original $CsPbBr_3$ QDs. (c) fs-TA spectra (excitation 400 nm) taken at several representative probe delays and (d) decay-associated spectra (DAS) for the radiation pressure $CsPbBr_3$ QDs.

the double peak of the features is also exhibited. We attribute the two positive photo-induced absorption (PA) profiles, labeled PA1 and PA2, to the lowest excitonic state and higher-lying excitonic states. What is more, the positive signals of the excited state absorption are rapidly established and maximized at the time of the high-energy or low-energy band. Then their decay trend of spectral behavior is the same as the original; we assign the positive signal of the low-energy band to the signal of the excited state absorption in the conduction band. The spectral changes of the PA peak near the high-energy band from 0 ps to 3 ps are attributed to the relaxation from free excitons (FEs) to STEs.

This fast exponential-decay component is expected to be due to the stimulated emission from free excitons and nonthermal STEs, in which the binding energy of the STEs remains as the kinetic energy of the lattice oscillation [57–59]. The decay kinetics is due to the intra-chain vibrational relaxation from free excitons to thermal STEs [57–59]. The transient absorbance changes are time resolved in the wide spectral region extending from 465 nm to 580 nm. The spectrum of the transient response represents the coupling between excitons and vibration of the lattice. Therefore, the transient absorption is shifted to a higher energy. The absorption peak near the high-energy band is assigned to the transitions from free exciton to STEs.

The resulting decay-associated spectra (DAS)-related characteristic time constants are shown in Table 2: $\tau_1 = 1.768$ ps $\pm$ 310 fs, $\tau_2 = 13.65$ ps $\pm$ 2.5 ps, and $\tau_3 = 121.9$ ps $\pm$ 20 ps for the original sample, while $\tau_1 = 644.0$ fs $\pm$ 0.0 fs, $\tau_2 = 12.80$ ps $\pm$ 2.4 ps, and $\tau_3 = 140.1$ ps $\pm$ 19 ps for the laser radiation pressure one. The τ_1, τ_2, and τ_3 components are known to account for the processes of intraband hot-exciton relaxation, exciton trapping to the band gap trap states, and exciton recombination, respectively [60], as schematically illustrated by the three downward-pointing black arrows in Fig. 4(c). Clearly, the former two processes get accelerated for the radiation pressure sample as compared to the original one. This effect can be understood as a result of the form of STE excited state [30]. As is known, strong coupling between electronic excitations and lattice vibrations is due to the form of STE, so radiation pressure coupling with the lattice of $CsPbBr_3$ QDs will cause increasing density of the lowest excitonic state. Thus, the increasing density of states would boost the coupling between the higher-lying excitonic state and the lowest excitonic state (i.e., the τ_1 process) and the coupling between the lowest excitonic state and the STE excited states (i.e., the τ_2 process) [60]. The long-lived component is considered to be induced by STE recombination with a lifetime much longer than 100 ps (a few tens of microseconds) (i.e., the τ_3 process) [61–63]. As the relative amplitude of radiation pressure $CsPbBr_3$ QDs is larger compared to that of original $CsPbBr_3$ QDs, population of STEs is greater in radiation

Table 2. Resulting DAS-Related Characteristic Time Constants of Original and Radiation Pressure $CsPbBr_3$ Samples

	τ_1 (ps)	τ_2 (ps)	τ_3 (ps)
Original QDs	1.768 ± 0.310	13.65 ± 2.5	121.9 ± 20
After radiation pressure	0.644 ± 0	12.80 ± 2.4	140.1 ± 19

pressure than original $CsPbBr_3$ QDs, which is responsible for the stronger PL. It suggests that more free excitons relax to self-trapping state due to structural contraction caused by radiation pressure. This leads to increased self-trapping state excitons and higher PLQYs in radiation pressure $CsPbBr_3$ QDs. This conclusion is consistent with the result of TR-PL decays. Therefore, these results suggest that radiation pressure induces contraction of the octahedral structure of perovskite, thereby improving the composite luminescence of STEs in $CsPbBr_3$ QDs.

To understand the impact of resistivity, carrier concentration, and mobility with laser radiation pressure, Hall effect measurements were performed on original and radiation pressure $CsPbBr_3$ samples in order to define any change in transport properties. It can be observed in Table 3 that there is a strong decrease in the resistivity from 210.2 Ω·cm for original $CsPbBr_3$ film to 61 Ω·cm of radiation pressure. The laser radiation pressure likely brings more free carriers resulting in the formation of more electrons. This is supported from the Hall effect measurement as the carrier density increases from 1.65×10^{14} cm^{-3} free electron for the original sample to 1.08×10^{15} cm^{-3} free electron under radiation pressure. The mobility of electrons drastically increases for radiation pressure, resulting in a low resistive original $CsPbBr_3$ film. Since the mobility increases, the carrier concentration decreases, as shown in Table 3.

In addition, surface roughness of the films is an important factor that affects their transport characteristics [64]. From the atomic force microscope (AFM) images shown in Fig. 8 in Appendix A.4, the surface roughness of the radiation pressure $CsPbBr_3$ films increases compared to the original. The root mean square roughness of the radiation pressure $CsPbBr_3$ films is 14.63 nm, while that of the original $CsPbBr_3$ films is 6.515 nm. The radiation pressure $CsPbBr_3$ films have increased surface roughness with higher free-carrier concentration corresponding to lower ρ and higher μ when compared to otherwise identically prepared films without radiation pressure [64,65].

Recently, it has been widely recognized that perovskite QDs appear as low-cost alternative materials to high-efficiency wide-color-gamut display technology [47,66,67]. Generally speaking, the key to wide-color-gamut backlight units for liquid crystal displays (LCDs) is the high-performance and high-efficiency green light generated by the perovskite quantum dots film (PQDF). In the present work, we focused on green QD backlight film, which is supposed to be applied in the display in combination with magenta LEDs (blue LEDs with a red KSF phosphor), and it is demonstrated that radiation pressure perovskite QDs have more promising luminescent properties than the original.

The green QD backlight films are encapsulated in a green perovskite QD layer sandwiched between fast-curing epoxy adhesive films, as shown in Fig. 5(a). The thickness of the QD layer itself is about 100 μm. The corresponding original and radiation pressure $CsPbBr_3$ QDs PL spectra under the same condition are shown in Figs. 5(b) and 5(c), respectively. As can be seen from the green peaks, the PL intensity of the radiation pressure $CsPbBr_3$ QDs is significantly higher than that of the original ones. Considering the high luminance with small currents, the current efficiencies of radiation pressure $CsPbBr_3$ LCDs exhibit a larger peak value of 0.441 $cd \cdot A^{-1}$, much higher than that of original $CsPbBr_3$ [Fig. 5(d)]. These devices also demonstrate higher power efficiency of 80.12 $lm \cdot W^{-1}$ than that of the radiation pressure $CsPbBr_3$ QDs device (73.05 $lm \cdot W^{-1}$) [Fig. 5(e)]. It confirms that radiation pressure perovskite QDs have excellent performance with respect to energy-saving aspects, which is thought being due to the very high quantum efficiency of radiation pressure perovskite QDs.

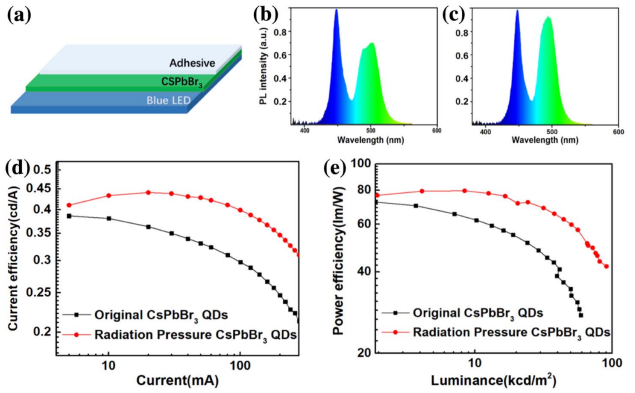

Fig. 5. (a) Schematic diagram of the configuration of the prototype LED device. Normalized emission PL spectra at an applied current of 20 mA using green emissive (b) original and (c) radiation pressure $CsPbBr_3$ QDs films. (d) Current efficiency of the devices as a function of current. (e) Power efficiency of the devices as a function of luminance.

Table 3. Transport Properties of Original and Radiation Pressure $CsPbBr_3$ Samples

	Resistivity (Ω·cm)	Mobility ($cm^2 \cdot v^{-1} \cdot s^{-1}$)	Density (cm^{-3})
Original QDs	210.2	1.61	5.6×10^{14}
After radiation pressure	61.0	3.83	1.08×10^{15}

3. EXPERIMENT

A. Preparation of $CsPbBr_3$ QDs and the Sample of $CsPbBr_3$ QDs Films

In this study, the perovskite QDs were synthesized by a chemical solution method and synthesized in an oxygen and water-free environment. Most chemicals used in the experiments, including Cs_2CO_3 (99.99%), octadecene (ODE, >90%), oleic acid (OA), oleylamine (OLA, 80%–90%), and $PbBr_2$ (99.999%), were purchased from Aladdin. Toluene (>99.5%) was purchased from Lingfeng Chemical Reagent Company (Shanghai, China). First, 0.0814 g cesium carbonate, 4 mL of octadecane, and 0.25 mL of OA were added into a 50 mL three-necked flask. Then they were heated under nitrogen to 120°C for 1 h until all the cesium carbonate reacted completely with OA to form Cs-oleate precursor. Then, 5 mL ODE, $PbBr_2$ (0.188 mmol), 0.5 mL of OLA, and 0.5 mL of OA were put into a 50 mL three-necked flask at the same time and heated under vacuum at 50°C for 1 h, and then heated under inert nitrogen gas to 120°C for 1 h. The temperature continued to rise to 160°C under a nitrogen

flow, and 0.4 mL Cs-oleate precursor solution preheated to 100°C was swiftly injected. After 5 s, the reaction mixture was cooled down to room temperature with an ice-water bath. The crude solution was centrifuged for 5 min at 11,000 r/min, with the supernatant discarded, and the precipitate redispersed in toluene to gain a stable $CsPbBr_3$ QDs solution. The precursor solution (10 mg/mL) was spin coated onto 30 mm diameter fused silica substrates at 1000 r/min for 60 s twice to obtain the sample of $CsPbBr_3$ QDs films, followed by drying at ambient conditions for 40 min.

B. Spectroscopy of the $CsPbBr_3$ QDs

The optical wavelength of 400 nm was generated by frequency doubling of output pulse (wavelength: 800 nm, repetition rate: 1 kHz, pulse width: 35 fs) from a regenerative amplifier using β-barium borate (BBO) crystal. The laser beam was focused vertically onto the $CsPbBr_3$ thin film via a cylindrical lens with focal length of 75 mm. The fluorescence spectra from the sample were collected by a spectrometer (Avavtes AvaSpec-3648-USB2-UA). UV–vis absorption spectra were recorded on a Zolix Omni-DR600-SZU spectrophotometer. The prepared samples in 30 mm quartz glasses were used to perform all UV–vis absorption and emission measurements. All the samples were measured at room temperature in air.

C. Structural and Chemical Characterization of the $CsPbBr_3$ QDs

TEM images of non-irradiated and irradiated $CsPbBr_3$ QDs were obtained on an FEI Tecnai G2 F30 transmission electron microscope operating at an acceleration voltage of 300 kV. XRD patterns of non-irradiated and irradiated $CsPbBr_3$ QDs were obtained using a Bruker AXS GADDS MWPC diffractometer equipped with Cu Kα X-ray radiation with a multi-wire proportional counter. The operation voltage and current were 40 kV and 25 mA, respectively. The 2θ range was from 10° to 60° in steps of 0.02°. SEM images and energy dispersive X-ray spectrometer (EDX) results were measured on Hitachi SU-70. The root mean square roughness was recorded by AFM (Asylum Research, MFP-3D Infinity, UK). The XPS measurement was carried out on a PHI QUANTERA SXM instrument. The X-ray spot size was 200 μm and X-ray power was 40 W. The survey spectra were taken with a pass energy of 280 eV and step size of 1 eV. The narrow spectra of each element were taken with a pass-energy of 55 eV and step size of 0.1 eV.

D. Femtosecond Transient-Absorption Spectroscopy and Time-Resolved Photoluminescence Spectroscopy

The fs (0.1 ps–8 ns) TAS used in this study is based on a regeneratively amplified Ti:sapphire laser system (Coherent, Legend, 800 nm, 35 fs, 5 mJ/pulse, and 1 kHz repetition rate) and the Helios spectrometer (Ultrafast Systems LLC). Pump pulse at 400 nm was generated by an optical parametric amplifier (OPA) (Coherent, OperA Solo); the pump beam diameter at the sample was 100 μm, corresponding to an excitation density of 8 $\mu J/cm^2$. A white-light continuum (from 420 nm to 780 nm) was generated by attenuating and focusing ~10 μJ of the 800 nm pulse into a sapphire window. The probe beam was focused with an Al parabolic reflector onto the sample (with a beam diameter of 50 μm at the sample). The probe beams were focused into a fiber-optics-coupled multichannel spectrometer with complementary metal-oxide-semiconductor (CMOS) sensors and detected at a frequency of 1 kHz. The delay between the pump and probe pulses was controlled by a direct-drive delay stage. The pump pulses were chopped by a synchronized chopper to 500 Hz, and the change in optical density at the sample resulting from the pump pulse was calculated. The instrument limited response time was 60 fs. Transient absorption data are calculated according to [68]

$$\log(I_0/I_{ex}),$$

where I_{ex} is the intensity of the probe light after the sample when the excitation light was incident on the sample, and I_0 is the intensity of probe light after the sample when the excitation light was blocked by an optical chopper. The samples were pumped at wavelength of 405 nm in the TR-PL experiments of the fluorescence lifetime spectrometer (PicoQuant Fluo Time 300). A visible streak camera system (Olympus) was used as a detector during the TR-PL experiments. The PLQYs of the samples were also measured by a fluorescence lifetime spectrometer (PicoQuant Fluo Time 300). The transport properties of the samples were measured by Nanometrics HL5500 Hall System. Current efficiency and power efficiency of the LCD devices were collected by using auto-temperature LED optoelectronic analyzer ATA-500 (the measurement equipment was designed by Everfine Photo-E-Info Co., Ltd.).

4. CONCLUSION

In summary, in this work, we have found that, similar to mechanical pressure, radiation pressure can also effectively enhance the PLQY of all-inorganic perovskite $CsPbBr_3$ QDs, so this work provides a more convenient method to improve the PL performance of all-inorganic perovskite $CsPbBr_3$ QDs. The increase of PLQY is due to the STE concentration caused by contraction octahedra structure under radiation pressure. We prove that radiation pressure does exist during this process, and based on the ultra-fast spectral dynamics synergy to explore the physical mechanism, it is confirmed that the radiation-pressure-induced luminescence can be attributed to the enhancement of the optical activity of the STE and the increase of the STEs' binding energy. The mechanisms underlying the increasing of self-trapping state excitons after radiation pressure were elucidated by studying the excited state dynamics processes. Furthermore, the liquid crystal display backlight film fabricated by adopting the radiation pressure $CsPbBr_3$ QDs showed more excellent performance with respect to energy-saving aspects than original QDs. This finding is likely to provide insight into the microscopic physiochemical mechanism and highly corroborate the strong correlations between structural contractions and the physical properties of QDs under radiation pressure.

APPENDIX A

1. Calculation of Radiation Pressure

According to Maxwell's theory of electromagnetism, an electromagnetic wave carries momentum, which will be transferred to an opaque surface it strikes [69–71]. The energy flux (irradiance) of a plane wave is calculated using the Poynting

Table 4. Radiation Pressure on Perfect Reflector at Normal Incidence ($\alpha = 0$)

Sample light intensity (W)	3	2	1.5	1	0.5	0.1
Radiation pressure (GPa)	0.38	0.30	0.25	0.18	0.12	0.06

Table 5. Different Magnitudes of Radiation Pressure on the Effect of PLQY of $CsPbBr_3$ QDs

Radiation pressure (GPa)	0.38	0.30	0.25	0.18	0.12	0.06
PLQY (%)	95	91	87	85	84	80

vector $S = E \cdot H$, whose magnitude we denote by S. S divided by the speed of light is the density of the linear momentum per unit area (pressure) of the electromagnetic field. That pressure is experienced as radiation pressure on the surface: $P = \frac{I_L}{c}$, where P is pressure (usually in Pascals), I_L is the incident irradiance intensity (usually in W/m^2), and c is the speed of light in vacuum (usually in m/s) [72]. If the surface is planar at an angle α to the incident wave, the intensity across the surface will be geometrically reduced by the cosine of that angle, and the component of the radiation force against the surface will also be reduced by the cosine of α, resulting in a pressure $P_{\text{incident}} = \frac{I_L}{c} \cos^2 \alpha$.

The momentum from the incident wave is in the same direction as that wave. But only the component of that momentum normal to the surface contributes to the pressure on the surface, as given above. The component of that force tangent to the surface is not called pressure.

It reflects the photon momentum obtained by the object per unit area per unit time. I_L, laser intensity, reflects the laser power P_L per unit area.

For a Gaussian beam, $I_L = I_0 \cdot \exp(-\frac{r^2}{r_0^2})$, where I_0 is the peak intensity, and r_0 is the focal spot radius:

$$P_L = \int I_L dS = 2\pi \int_0^{p_0} I_0 \cdot \exp\left(-\frac{r^2}{r_0^2}\right) \cdot r dr = I_0 \cdot \pi r_0^2.$$

Peak light intensity at a certain location is $I_0 = \frac{P_L}{\pi r_0^2}$.

The time envelope is a flat-top pulse envelope; laser energy is $E_L = P_L \cdot \tau$, where τ is pulse width. Corresponding peak light intensity is $I_0 = \frac{P_L}{\pi r_0^2} = \frac{E_L}{\pi r_0^2 \cdot \tau}$.

Corresponding light pressure is $P = \frac{I_0}{c}(R = 0) = \frac{E_L}{\pi r_0^2 \cdot \tau \cdot c}$.

When the time envelope is Gaussian,

$$P_L = P_0 \cdot \exp\left(-\frac{t^2}{\tau_0^2}\right), \qquad E_L = P_0 \cdot \sqrt{\pi} \cdot \tau,$$

corresponding to the peak light pressure $P = \frac{I_0}{c} = \frac{E_L}{\pi r_0^2 \cdot \sqrt{\pi} \cdot \tau \cdot c}$.

Based on the above formula, we calculate the magnitude of the radiation pressure: the average pressure is small but the peak radiation pressure is large. The theoretical calculation section, as shown in Table 4, is the pressure on the surface of the material under different radiation pressures. In this experiment, we use normal incidence.

2. SEM Images of the Original $CsPbBr_3$ QDs Thin Films

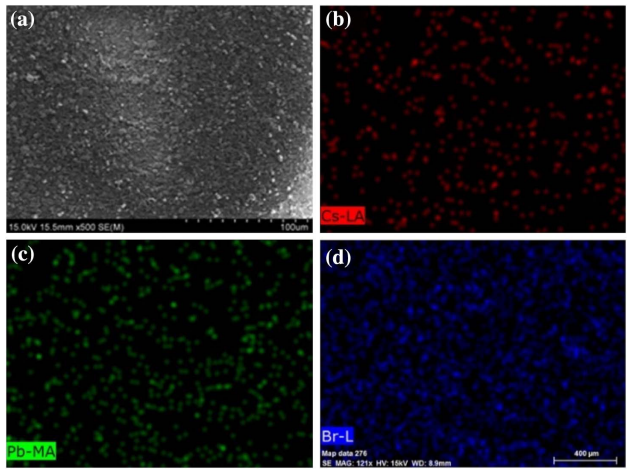

Fig. 6. (a) SEM image of $CsPbBr_3$ QDs thin film. (b)–(d) Elemental mappings of Cs, Pb, and Br in $CsPbBr_3$ QDs.

3. TEM and High-Resolution TEM Images of Radiation Pressure $CsPbBr_3$ QDs Thin Film

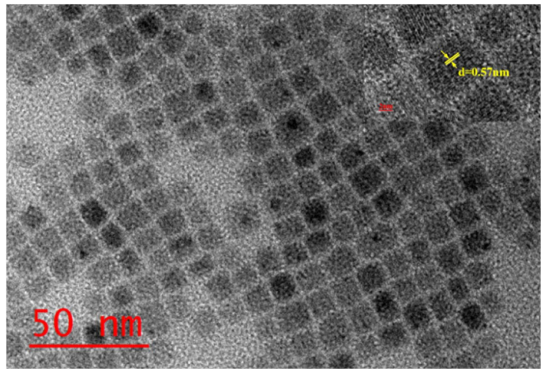

Fig. 7. TEM and high-resolution TEM images of radiation pressure $CsPbBr_3$ QDs thin film.

4. AFM Images of the Original and Radiation Pressure $CsPbBr_3$ QDs Thin Film

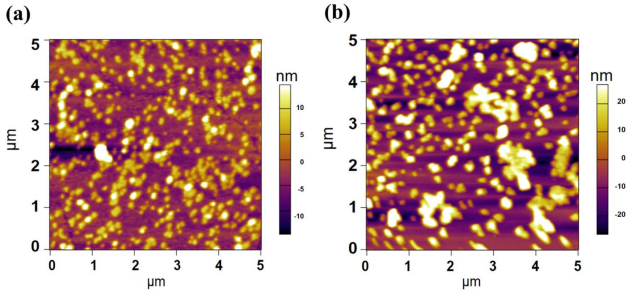

Fig. 8. Comparison of AFM images of (a) the original and (b) radiation pressure $CsPbBr_3$ films. The root mean square roughness is 6.615 nm and 14.63 nm, respectively.

Funding. National Key R&D Program of China (2016YFA041100); China Postdoctoral Science Foundation (2016M592528); Natural Science Foundation of Guangdong Province (2017A030310130); National Natural Science Foundation of China (NSFC) (11704285, 61575129, 61805156); Science Technology Innovation Committee Foundation of Shenzhen (JCYJ20160328144942069).

REFERENCES

1. D. Mihalas, ed., *Stellar Atmospheres*, 2nd ed. (W. H. Freeman & Co., 1978).
2. A. S. Eddington and A. S. Eddington, *The Internal Constitution of the Stars* (Cambridge University, 1988).
3. S. Chandrasekhar, *Radiative Transfer* (Courier Corporation, 2013).
4. O. Arcizet, P.-F. Cohadon, and T. Briant, "Radiation-pressure cooling and optomechanical instability of a micromirror," Nature **444**, 71–74 (2006).
5. S. Gigan, H. R. Boehm, and M. Paternostro, "Self-cooling of a micromirror by radiation pressure," Nature **444**, 67–70 (2006).
6. A. Henig, S. Steinke, and M. Schnuerer, "Radiation-pressure acceleration of ion beams driven by circularly polarized laser pulses," Phys. Rev. Lett. **103**, 245003 (2009).
7. B.-W. Max and K. J. Chau, "Simulations of radiation pressure experiments narrow down the energy and momentum of light in matter," Rep. Prog. Phys. **78**, 122401 (2015).
8. A. Schliesser, P. Del'Haye, and N. Nooshi, "Radiation pressure cooling of a micromechanical oscillator using dynamical backaction," Phys. Rev. Lett. **97**, 243905 (2006).
9. A. S. Mancini, V. Giovannetti, and D. Vitali, "Entangling macroscopic oscillators exploiting radiation pressure," Phys. Rev. Lett. **88**, 120401 (2002).
10. T. J. Kippenberg, H. Rokhsari, and T. Carmon, "Analysis of radiation-pressure induced mechanical oscillation of an optical microcavity," Phys. Rev. Lett. **95**, 033901 (2005).
11. A. Ashkin, "Applications of laser-radiation pressure," Science **210**, 1081–1088 (1980).
12. A. Kojima, K. Teshima, Y. Shirai, and T. Miyasaka, "Organometal halide perovskites as visible-light sensitizers for photovoltaic cells," J. Am. Chem. Soc. **131**, 6050–6051 (2009).
13. J.-H. Im, C.-R. Lee, J.-W. Lee, S.-W. Park, and N.-G. Park, "6.5% efficient perovskite quantum-dot-sensitized solar cell," Nanoscale **3**, 4088–4093 (2011).
14. I. Chung, B. Lee, J. He, R. P. H. Chang, and M. G. Kanatzidis, "All-solid-state dye-sensitized solar cells with high efficiency," Nature **485**, 486–489 (2012).
15. M. M. Lee, J. Teuscher, T. Miyasaka, T. N. Murakami, and H. J. Snaith, "Efficient hybrid solar cells based on meso-superstructured organometal halide perovskites," Science **338**, 643–647 (2012).
16. O. Malinkiewicz, A. Yella, Y. H. Lee, G. M. Espallargas, M. Graetzel, M. K. Nazeeruddin, and H. J. Bolink, "Perovskite solar cells employing organic charge-transport layers," Nat. Photonics **8**, 128–132 (2014).
17. M. Liu, M. B. Johnston, and H. J. Snaith, "Efficient planar heterojunction perovskite solar cells by vapour deposition," Nature **501**, 395–398 (2013).
18. J. Burschka, N. Pellet, S.-J. Moon, R. Humphry-Baker, P. Gao, M. K. Nazeeruddin, and M. S. Grätzel, "Deposition as a route to high-performance perovskite-sensitized solar cells," Nature **499**, 316–319 (2013).
19. D. Liu and T. L. Kelly, "Perovskite solar cells with a planar heterojunction structure prepared using room-temperature solution processing techniques," Nat. Photonics **8**, 133–138 (2014).
20. J.-W. Lee, D.-J. Seol, A.-N. Cho, and N.-G. Park, "High-efficiency perovskite solar cells based on the black polymorph of $Hc(NH_2)_2PbI_3$," Adv. Mater. **26**, 4991–4998 (2014).
21. H. Zhou, Q. Chen, G. Li, S. Luo, T. Song, H.-S. Duan, Z. Hong, J. You, Y. Liu, and Y. Yang, "Photovoltaics interface engineering of highly efficient perovskite solar cells," Science **345**, 542–546 (2014).
22. R. E. Beal, D. J. Slotcavage, T. Leijtens, A. R. Bowring, R. A. Belisle, W. H. Nguyen, G. F. Burkhard, E. T. Hoke, and M. D. McGehee, "Cesium lead halide perovskites with improved stability for tandem solar cells," J. Phys. Chem. Lett. **7**, 746–751 (2016).
23. M. Kulbak, S. Gupta, N. Kedem, I. Levine, T. Bendikov, G. Hodes, and D. Cahen, "Cesium enhances long-term stability of lead bromide perovskite-based solar cells," J. Phys. Chem. Lett. **7**, 167–172 (2016).
24. J. Song, J. Li, X. Li, L. Xu, Y. Dong, and H. Zeng, "Quantum dot light-emitting diodes based on inorganic perovskite cesium lead halides ($CsPbX_3$)," Adv. Mater. **27**, 7162–7167 (2015).
25. N. Yantara, S. Bhaumik, F. Yan, D. Sabba, H. A. Dewi, N. Mathews, P. P. Boix, H. V. Demir, and S. Mhaisalkar, "Inorganic halide perovskites for efficient light-emitting diodes," J. Phys. Chem. Lett. **6**, 4360–4364 (2015).
26. C. L. Li, Z. G. Zang, W. Chen, Z. P. Hu, X. S. Tang, W. Hu, K. Sun, X. M. Liu, and W. M. Chen, "Highly pure green light emission of perovskite $CsPbBr_3$ quantum dots and their application for green light-emitting diodes," Opt. Express **24**, 15071–15078 (2016).
27. C. C. Stoumpos, C. D. Malliakas, J. A. Peters, Z. Liu, M. Sebastian, J. Im, T. C. Chasapis, A. C. Wibowo, D. Y. Chung, A. J. Freeman, and B. W. Wessels, "Crystal growth of the perovskite semiconductor $CsPbBr_3$: a new material for high-energy radiation detection," Cryst. Growth Des. **13**, 2722–2727 (2013).
28. C. L. Lia, C. Hana, Y. B. Zhangb, Z. G. Zanga, M. Wanga, X. S. Tanga, and J. Dub, "Enhanced photoresponse of self-powered perovskite photodetector based on ZnO nanoparticles decorated $CsPbBr_3$ films," Sol. Energy Mater. Sol. Cells **172**, 341–346 (2017).
29. C. Han, C. L. Li, Z. G. Zang, M. Wang, K. Sun, X. S. Tanga, and J. Dub, "Tunable luminescent $CsPb_2Br_5$ nanoplatelets: applications in light-emitting diodes and photodetectors," Photon. Res. **5**, 473–480 (2017).
30. P. Ramasamy, D. H. Lim, B. Kim, S. H. Lee, M. S. Lee, and J. S. Lee, "All-inorganic cesium lead halide perovskite nanocrystals for photodetector applications," Chem. Commun. **52**, 2067–2070 (2016).
31. X. He, P. Liu, H. Zhang, Q. Liao, J. Yao, and H. Fu, "Patterning multicolored microdisk laser arrays of cesium lead halide perovskite," Adv. Mater. **29**, 1604510 (2017).
32. Y. Wang, X. Li, J. Song, L. Xiao, H. Zeng, and H. Sun, "AllInorganic colloidal perovskite quantum dots: a new class of lasing materials with favorable characteristics," Adv. Mater. **27**, 7101–7108 (2015).
33. C. L. Lia, Z. G. Zanga, C. Hana, Z. P. Hua, X. S. Tanga, J. Dub, Y. Lengb, and K. Sunc, "Highly compact $CsPbBr_3$ perovskite thin films decorated by ZnO nanoparticles for enhanced random lasing," Nano Energy **40**, 195–202 (2017).
34. Q. Zhang, R. Su, W. Du, X. Liu, L. Zhao, S.-T. Ha, and Q.-H. Xiong, "Advances in small perovskite-based lasers," Small Methods **1**, 1700163 (2017).
35. X. Chen, H. Hu, Z. Xia, W. Gao, W. Gou, Y. Qu, and Y. Ma, "$CsPbBr_3$ perovskite nanocrystals as highly selective and sensitive spectrochemical probes for gaseous Hcl detection," J. Mater. Chem. C **5**, 309–313 (2017).
36. A. H. Ip, A. Kiani, I. J. Kramer, O. Voznyy, H. F. Movahed, L. Levina, M. M. Adachi, S. Hoogland, and E. H. Sargent, "Infrared colloidal quantum dot photovoltaics via coupling enhancement and agglomeration suppression," ACS Nano **9**, 8833–8842 (2015).
37. G. H. Carey, A. L. Abdelhady, Z. J. Ning, S. M. Thon, O. M. Bakr, and E. H. Sargent, "Colloidal quantum dot solar cells," Chem. Rev. **115**, 12732–12763 (2015).
38. D. Rossi, D. Parobek, Y. Dong, and D.-H. Son, "Dynamics of exciton-Mn energy transfer in Mn-doped $CsPbCl_3$ perovskite nanocrystals," J. Phys. Chem. C **121**, 17143–17149 (2017).
39. W. Nie, H. Tsai, R. Asadpour, J.-C. Blancon, A. J. Neukirch, G. Gupta, J. J. Crochet, M. Chhowalla, S. Tretiak, M. A. Alam, H.-L. Wang, and A. D. Mohite, "High-efficiency solution-processed perovskite solar cells with millimeter-scale grains," Science **347**, 522–525 (2017).
40. D. Bi, C. Yi, J. Luo, J.-D. DÉCoppet, F. Zhang, S. M. Zakeeruddin, X. Li, A. Hagfeldt, and M. Grätzel, "Polymer-templated nucleation and crystal growth of perovskite films for solar cells with efficiency greater than 21%," Nat. Energy **1**, 16142 (2016).

41. Y. Zhou, J. Chen, O. M. Bakr, and H. Sun, "Metal-doped lead halide perovskites: synthesis, properties, and optoelectronic applications," Chem. Mater. **30**, 6589–6613 (2018).
42. Z. Yong, S. Guo, J. Ma, J. Zhang, Z. Li, Y. Chen, B. Zhang, Y. Zhou, J. Shu, J. Gu, L. Zheng, O. M. Bakr, and H. Sun, "Doping-enhanced short-range order of perovskite nanocrystals for near-unity violet luminescence quantum yield," J. Am. Chem. Soc. **140**, 9942–9951 (2018).
43. Y. Wu, C. Wei, X. Li, Y. Li, S. Qiu, W. Shen, B. Cai, Z. Sun, D. Yang, Z. Deng, and H. Zeng, "*In situ* passivation of $PbBr_6^{4-}$ octahedra toward blue luminescent $CsPbBr_3$ nanoplatelets with near 100% absolute quantum yield," ACS Energy Lett. **3**, 2030–2037 (2018).
44. Z. Ma, Z. Liu, S. Lu, L. Wang, X. Feng, D. Yang, K. Wang, G. Xiao, L. Zhang, S. Redfern, and B. Zou, "Pressure-induced emission of cesium lead halide perovskite nanocrystals," Nat. Commun. **9**, 4506 (2018).
45. N. Yasutaka, K. Kimball, R. Tan, R. Li, Z. Wang, and O. Chen, "Nanocube superlattices of cesium lead bromide perovskites and pressure-induced phase transformations at atomic and mesoscale levels," Adv. Mater. **29**, 1606666 (2017).
46. G. Xiao, Y. Cao, G. Qi, L. Wang, C. Liu, Z. Ma, X. Yang, Y. Sui, W. Zheng, and B. Zou, "Pressure effects on structure and optical properties in cesium lead bromide perovskite nanocrystals," J. Am. Chem. Soc. **139**, 10087–10094 (2017).
47. L. Protesescu, S. Yakunin, M. I. Bodnarchuk, F. Krieg, R. Caputo, C. H. Hendon, R. X. Yang, A. Walsh, and M. V. Kovalenko, "Nanocrystals of cesium lead halide perovskites ($CsPbX_3$, X = Cl, Br, and I): novel optoelectronic materials showing bright emission with wide color gamut," Nano Lett. **15**, 3692–3696 (2015).
48. K. Tanimura and N. Itoh, "Relaxation of excitons perturbed by self-trapped excitons in RbI: evidence for exciton fusion in inorganic solids with strong electron-phonon coupling," Phys. Rev. Lett. **64**, 1429–1432 (1990).
49. M. Yoshizawa, Y. Hattori, and T. Kobayashi, "Nonlinear optical susceptibilities of epitaxially grown polydiacetylene measured by femtosecond time-resolved spectroscopy," Phys. Rev. B **47**, 3882–3889 (1993).
50. M. Yoshizawa, K. Nishiyama, M. Fujihira, and T. Kobayashi, "Exciton transition energy and temperature dependence of ultrafast relaxation of self-trapped excitons in polydiacetylenes," Chem. Phys. Lett. **207**, 461–467 (1993).
51. M. P. Prange, R. M. Van Ginhoven, N. Govind, and F. Gao, "Formation, stability, and mobility of self-trapped excitations in NaI and $NaI_{1-x}Tl_x$ from first principles," Phys. Rev. B **87**, 115101 (2013).
52. Y. Liu, P. Chen, Z. H. Wang, F. Bian, L. Lin, S. J. Chang, and G. G. Mu, "Efficient two-photon absorption of CdSe-CdS/Zns core-multishell quantum dots under the excitation of near-infrared femtosecond pulsed laser," Laser Phys. **19**, 1886–1890 (2009).
53. H. Cho, S.-H. Jeong, M. H. Park, Y.-H. Kim, C. Wolf, C.-L. Lee, J. H. Heo, A. Sadhanala, N. Myoung, S. Yoo, S. H. Im, R. H. Friend, and T.-W. Lee, "Overcoming the electroluminescence efficiency limitations of perovskite light-emitting diodes," Science **350**, 1222–1225 (2015).
54. J. Xing, X. F. Liu, Q. Zhang, S. T. Ha, Y. W. Yuan, C. Shen, T. C. Sum, and Q. H. Xiong, "Vapor phase synthesis of organometal halide perovskite nanowires for tunable room-temperature nanolasers," Nano Lett. **15**, 4571–4577 (2015).
55. A. Yasuda, M. Yoshizawaand, and T. Kobayashi, "Fluorescence spectrum of a blue-phase polydiacetylene obtained by probe saturation spectroscopy," Chem. Phys. Lett. **209**, 281–286 (1993).
56. N. Mondal and A. Samanta, "Complete ultrafast charge carrier dynamics in photo-excited all-inorganic perovskite nanocrystals ($CsPbX_3$)," Nanoscale **9**, 1878–1885 (2017).
57. M. Yoshizawa, A. Yasuda, and T. Kobayashi, "Ultrafast optical response in polydiacetylenes and polythiophenes," Appl. Phys. B **53**, 296–307 (1991).
58. T. Kobayashi and M. Yoshizawa, "Femtosecond nonlinear response of polydiacetylenes and polythiophenes," Synth. Metals **43**, 3129–3134 (1991).
59. T. Kobayashi, "Ultrafast relaxation in conjugated polymers," J. Lumin. **53**, 159–164 (1992).
60. J. Yao, J. Ge, B. Han, K. Wang, H. Yao, H. Yu, J. Li, B. Zhu, J. Song, C. Chen, Q. Zhang, H. Zeng, Y. Luo, and S. Yu, "Ce^{3+}-doping to modulate photoluminescence kinetics for efficient $CsPbBr_3$ nanocrystals based light-emitting diodes," J. Am. Chem. Soc. **140**, 3626–3634 (2018).
61. T. Kobayashi and H. Ikeda, "Dependence of the spectrum and decay of transient photoinduced reflectance change on excitation wavelength and intensity in polydiacetylene single crystals," Chem. Phys. Lett. **133**, 54–58 (1987).
62. T. Kobayashi and H. Ikeda, "Dependence of excitation wavelength and intensity on the spectrum and decay of the time-resolved reflectance change of polydiacetylene single crystals," Synth. Metals **18**, 441–446 (1987).
63. T. Kobayashi, H. Ikeda, S. Tstmeyuki, and T. Kotaka, "$T_n \leftarrow T_1$ absorption spectra of urethane substituted polydiacetylene in solutions at several pH values," Chem. Phys. Lett. **116**, 515–520 (1985).
64. P. Uprety, B. Macco, M. M. Junda, C. R. Grice, W. M. M. Kessels, and N. J. Podraza, "Optical and electrical properties of H_2 plasma-treated ZnO films prepared by atomic layer deposition using supercycles," Mater. Sci. Semi. Proc. **84**, 91–100 (2018).
65. B. Macco, H. C. M. Knoops, M. A. Verheijen, W. Beyer, M. Creatore, and W. M. M. Kessels, "Atomic layer deposition of high-mobility hydrogen-doped zinc oxide," Sol. Energ. Mater. Sol. Cells **173**, 111–119 (2017).
66. F. Zhang, H. Zhong, C. Chen, X.-G. Wu, X. Hu, H. Huang, J. Han, B. Zou, and Y. Dong, "Brightly luminescent and color-tunable colloidal $CH_3NH_3PbX_3$ (X = Br, I, Cl) quantum dots: potential alternatives for dsplay technology," ACS Nano **9**, 4533–4542 (2015).
67. Z. Bai and H. Zhong, "Halide perovskite quantum dots: potential candidates for display technology," Sci. Bull. **60**, 1622–1624 (2015).
68. T. C. Sum, N. Mathews, G. C. Xing, S. S. Lim, W. K. Chong, D. Giovanni, and H. A. Dewi, "Spectral features and charge dynamics of lead halide perovskites: origins and interpretations," Acc. Chem. Res. **49**, 294–302 (2016).
69. H. Polaert, G. Grehan, and G. Gouesbet, "Forces and torques exerted on a multilayered spherical particle by a focused Gaussian bean," Opt. Commun. **155**, 169–179 (1998).
70. J. P. Barton, "Internal and near-surface electromagnetic fields for a spherical particle irradiated by a focused light beam," J. Appl. Phys. **64**, 1632–1639 (1998).
71. J. P. Barton and D. R. Alexander, "Fifth-order corrected electromagnetic field components for a fundamental Gaussian beam," J. Appl. Phys. **66**, 2800–2802 (1989).
72. E. F. Nichols and G. F. Hull, "The pressure due to radiation," Astrophys. J. **17**, 315–351 (1903).